

Article

Martensitic Transformation, Magnetic and Mechanical Characteristics in Unidirectional Ni–Mn–Sn Heusler Alloy

Haodong Sun¹, Chao Jing^{1,*}, Hui Zeng¹, Yuan Su¹, Siyuan Yang², Yuanlei Zhang³ , Tarek Bachagha^{1,2,4} , Ting Zhou², Long Hou² and Wei Ren^{1,2,4}¹ Department of Physics, Shanghai University, Shanghai 200444, China² State Key Laboratory of Advanced Special Steel, School of Materials Science and Engineering, Shanghai University, Shanghai 200072, China³ College of Physics and Electronic Engineering, Qujing Normal University, Qujing 655011, China⁴ Materials Genome Institute, Shanghai Key Laboratory of High Temperature Superconductors, International Centre of Quantum and Molecular Structures, Shanghai University, Shanghai 200444, China* Correspondence: cjing@staff.shu.edu.cn

Abstract: A textured structure of Ni–Mn–Sn Heusler alloy with [001] preferred orientation has been grown by the directional solidification method. The crystal exhibits a single austenite phase $L2_1$ cubic structure ($a = 5.997 \text{ \AA}$) at room temperature. Magnetization and electronic transport measurements reveal the phase transformation characteristics. The maximum values of magnetic entropy change determined by Maxwell's thermodynamic relation during the structural and magnetic phase transformations are $3.5 \text{ J/kg}\cdot\text{K}$ and $-4.1 \text{ J/kg}\cdot\text{K}$, and the total effective refrigerant capacity reaches about 314 J/kg (5 T). The evident reduction in hysteresis loss and broad operating temperature window provide a greater prospect for improving the cyclic stability of refrigeration and optimizing the application of such a magnetic refrigeration material. Both magnetoresistance (-18% , 5 T) and exchange bias field (302 Oe, 2 K) have also been investigated to understand the nature of phase transformations and exchange interactions. Furthermore, as the material exhibits excellent mechanical properties (1068 MPa, 9.0%), our experimental results provide a new reference for the application of Ni–Mn–Sn Heusler alloys.

Keywords: Ni–Mn–Sn Heusler; directional solidification; martensitic transformation; magnetocaloric effect; mechanical properties



Citation: Sun, H.; Jing, C.; Zeng, H.; Su, Y.; Yang, S.; Zhang, Y.; Bachagha, T.; Zhou, T.; Hou, L.; Ren, W. Martensitic Transformation, Magnetic and Mechanical Characteristics in Unidirectional Ni–Mn–Sn Heusler Alloy.

Magnetochemistry **2022**, *8*, 136.
<https://doi.org/10.3390/magnetochemistry8100136>

Academic Editor: José Luis Sánchez Llamazares

Received: 19 September 2022

Accepted: 18 October 2022

Published: 21 October 2022

Publisher's Note: MDPI stays neutral with regard to jurisdictional claims in published maps and institutional affiliations.



Copyright: © 2022 by the authors. Licensee MDPI, Basel, Switzerland. This article is an open access article distributed under the terms and conditions of the Creative Commons Attribution (CC BY) license (<https://creativecommons.org/licenses/by/4.0/>).

1. Introduction

The Ni–Mn–(In, Sn, Sb) Heusler alloys have recently been followed with interest owing to the strong coupling between magnetic and structural free degrees [1,2]. These metamagnetic shape memory alloys (MSMAs) would undergo martensitic transformation (MT) at a certain temperature. Such a magneto-structural phase transformation would result in unique functional properties, including magnetic field-induced strain (MFIS) [3], direct (MCE) and inverse magnetocaloric effect (IMCE) [4–6], exchange bias (EB) [7,8], magnetoresistance effect (MR) [9,10], etc. These properties are being further developed for potential future applications in magnetic refrigeration, information storage, and sensing drives. Among the MCE, Ni–Mn-based Heusler alloys have a broader application prospect compared to some rare-earth-based compounds because of their high magnetic refrigeration operating temperature (near room temperature) and lower cost compared to rare earth elements [11–13]. Many researchers have carried out a series of studies on Ni–Mn-based Heusler alloys and found that MT in such alloys is very sensitive to composition. One widely accepted explanation is the adjustment of valence electron concentration (e/a) to the phase transformation, as the MT temperature would increase linearly with the increase of e/a within a certain range [14,15]. The parent phase of the alloys is usually an $L2_1$ cubic structure with high symmetry at high temperatures. During the cooling procedure,

the alloys usually change into the $L1_0$ martensite phase with low symmetry or present several modulation structures of martensite variants [16], which give rise to abundant magnetic properties. For instance, the Heusler alloys typically exhibit the coexistence of ferromagnetic (FM), antiferromagnetic (AFM), superferromagnetic (SFM), or superspin glass (SSG) once the martensite transition has occurred [17–20]. The various potential complex magnetic states arise from the competing interactions between Mn atoms, which is a key technical origin of the EB effect.

At present, researchers mainly explore and improve the physical properties of Heusler materials by adjusting the proportion of elements and substitution doping of the fourth element [21–24]. Apart from these, there could also be other extrinsic factors for the properties of materials, such as preparation methods and pretreatment conditions [25–27]. The microstructure and magnetic characteristics of Heusler alloys prepared by traditional metallurgy, thin film techniques [28,29], or melt spinning [30] have been reported by many investigators. However, information about Heusler single crystal or unidirectional crystal is relatively limited so far. Single crystals of ferromagnetic shape memory alloys are very fascinating and significant from both a foundational and an application viewpoint. For example, Ni–Mn–Ga single crystal exhibits large strain due to a lack of independent crystals and grain boundaries with different orientations [31]. In addition, enhanced MCE was also reported in the Ni–Mn–Sn unidirectional crystal [32]. In the present paper, a highly [001] orientated Ni–Mn–Sn Heusler crystal was prepared by the directional solidification method. The crystal structural, magnetic, electrical, and mechanical characteristics of the material were studied so as to regulate the microstructure and physical properties by crystal growth and extend the application prospects of such alloys.

2. Materials and Methods

Highly textured $\text{Ni}_{50}\text{Mn}_{36}\text{Sn}_{14}$ Heusler alloy was grown by Bridgman type directional solidification method from a master alloy. The as-cast ingot was prepared by repeated melting of high purity Ni, Mn, and Sn (99.99%, Alfa Aesar, Ward Hill, MA, USA) under argon atmosphere (an extra 2% Mn was added on account of its volatility), and it then was melted and subsequently suctioned into a copper mold to get a precursor rod. The rod was placed into a corundum crucible in a crystal growing furnace and heated to a maximum of about 1723 K in an atmosphere of argon. After holding the temperature for 30 min, the crucible was pulled into the Ga–In–Sn liquid metal at the speed of 50 $\mu\text{m}/\text{s}$ to obtain the final sample. Next, the obtained sample rod was annealed at 1173 K for 24 h, followed by quenching by ice water.

The microstructure of the sample was observed by an optical metalloscope (Leica, Wetzlar, Germany); the chemical composition and crystal orientation were characterized by an X-ray energy dispersive spectrometer (EDS) (EDAX, Pleasanton, CA, USA) and Hikari electron backscattering diffraction (EBSD, Macherio, Italy) high-speed probe on a scanning electron microscope (SEM, QUANTA 450) (Hitachi, Ibaraki, Japan), respectively. At room temperature, X-ray diffraction (XRD, D2-Phaser) (Bruker, Karlsruhe, Germany) with $\text{Cu-K}\alpha$ radiation was performed to identify the crystal structure, and Rietveld refinement was carried out according to the XRD result using the Fullprof software package. A small rectangular sample (virgin sample) was cut in the sample rod for magnetic and electrical transmission measurements. Magnetic and electrical transmission data were collected by a physical property measurement system (PPMS-14) (Quantum Design, San Diego, CA, USA) with associated integrated accessories. Applying a magnetic field is parallel to the crystal growth direction (CGD) in each magnetization measurement. For resistance measurement, the electric current and the magnetic field were parallel and perpendicular to CGD, respectively. In the compression test, a sample with a diameter of 3 mm and a length of 7 mm was compressed to fracture with a constant speed of 0.15 mm/min at room temperature using an MTS809 material testing machine (MTS, Eden Prairie, MN, USA).

3. Results and Discussion

3.1. Microstructure and Crystal Structure

The longitudinal and transverse microstructures of Ni–Mn–Sn crystal at room temperature are shown in Figure 1a,b respectively. The images show that the typical microstructure characterized by coarse dendrites with a diameter of about 0.25 mm in the sample, and the crystal growth direction deviates slightly from the solidification direction (SD). The main reason for this deviation can be attributed to the mechanical vibration of the lower driving equipment when the crystal grows in the crucible. In addition, complete austenite phase exists in the sample, which is also confirmed by the EBSD analysis.

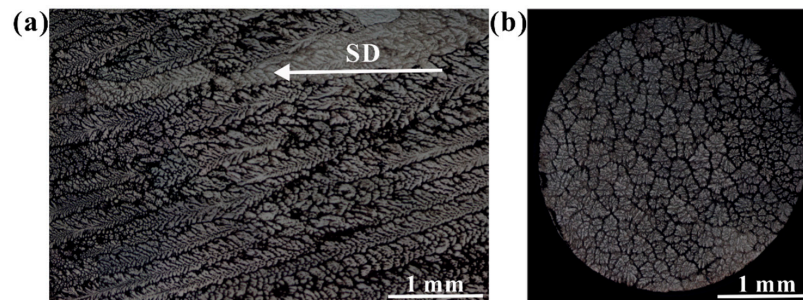


Figure 1. Microstructure of stable growth region of Ni–Mn–Sn crystal: (a) Longitudinal section. (b) Cross-section.

Figure 2a shows the orientation map of the longitudinal section of the alloy at room temperature; the EBSD map was indexed in the light of the austenite structure and shows that there is obvious $[001]_A$ preferred orientation in crystal growth. The large temperature gradient along SD during crystal growth would result in such a microstructure feature. According to the (001) pole figure (see Figure 2b) derived from the EBSD map, the high texture in the sample deviates from axis A2 (i.e., SD) by about 20° , which also corresponds to the metallographic figure. It is also worth noting that the microstructure with high texture is very beneficial to improving the mechanical properties and thermal effects of materials [33–35]. Furthermore, the elements and distribution of the sample were checked by EDS (as Figure 2c) and the homogeneity was confirmed. In order to observe the variation of the content of individual constituent elements in the sample, compositional distribution was measured by EDS along the CGD, as shown in Figure 2d, which indicates that the sample shows a stable expected composition ratio in a large range. Therefore, the high quality of the $[001]$ -oriented crystal was confirmed.

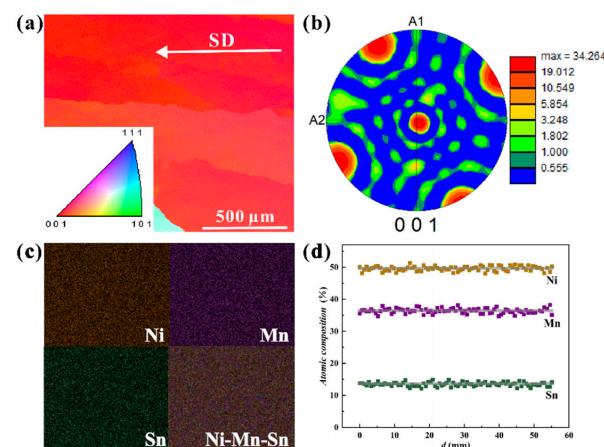


Figure 2. Scanning electron microscopy on the Ni–Mn–Sn crystal. (a) EBSD orientation mapping of the longitudinal section expressed in inverse pole figure (IPF) mode. (b) (001) pole figure (PF) along the SD calculated from the orientation mapping. (c) EDS elemental maps. (d) Compositional distribution along the crystal growth direction.

Figure 3 depicts the XRD pattern of the $\text{Ni}_{50}\text{Mn}_{36}\text{Sn}_{14}$ crystal measured at room temperature, and the inset on the upper right is the unit cell of the $\text{Ni}_{50}\text{Mn}_{36}\text{Sn}_{14}$ crystal. Rietveld refinement ($R_{\text{wp}} = 12.61\%$) suggests that the crystal presents a single austenite phase, i.e., $L2_1$ cubic (space group $Fm\bar{3}m$) structure with the lattice parameters of $a = 5.997 \text{ \AA}$ and $\alpha = 90^\circ$.

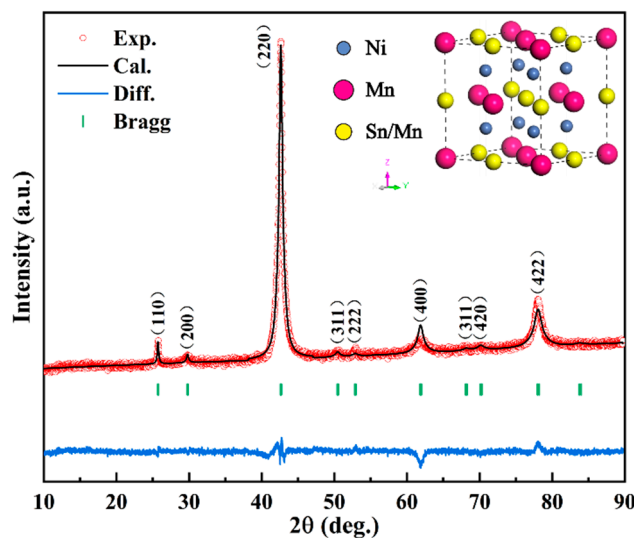


Figure 3. X-ray diffraction pattern for the Ni–Mn–Sn crystal measured at room temperature. Inset: unit cell of Ni–Mn–Sn crystal.

3.2. Magnetic Properties

The phase transformations and magnetic features of the virgin sample can be represented by thermomagnetic curves of 500 Oe magnetic field, as shown in Figure 4. It can be found that the magnetic transformation temperature of the austenite phase (Curie temperature T_C^A) is about 325 K. Below T_C^A , the abrupt changes of magnetization are observed in the range 230 K (M_S)–170 K (M_f) and 195 K (A_S)–255 K (A_f) corresponding to MT and reverse MT, respectively. Furthermore, field cooling (FC) and zero-field cooling (ZFC) curves split at low temperature and there is an inflection point called blocking temperature T_B (~65 K) in the ZFC curve, which indicates the existence of magnetically inhomogeneous states. This is generally related to competition between FM and AFM systems.

After determining the characteristic temperatures of phase transformation from the thermomagnetic curves, the sample was then subjected to isothermal magnetization measurements at different temperatures. The isothermal magnetization measurements around MT and around the magnetic transformation are demonstrated in Figure 5a,b, respectively. Initially, the sample was cooled from 300 K to 100 K to ensure that it was in a complete martensitic phase before each M - H curve was measured. This step is to prevent the possible influence of residual austenite induced by magnetic field during the previous magnetization measurement. This was followed by heating up to the desired temperature to get the isotherms with the magnetic field increased to 5 T. From Figure 5a, the curves show FM behavior over the measured temperature range. It can be seen that there is an inflection point in the curve during the increase of the magnetic field, and this change of magnetization state corresponds to the reverse MT of field-induced martensite to austenite transformation. Due to the thermal hysteresis of first-order phase transformation, the field down curve does not coincide with field up, and hysteresis loss (HL) occurs. In addition, the magnetization intensity of the sample varies little over a large temperature range, increasing from 47.1 to 72.1 emu/g, such that a smaller magnetic entropy change (ΔS_M) can be expected. As the temperature rises further, the austenite undergoes a magnetic transformation, the magnetization intensity decreases, and the HL disappears (Figure 5b).

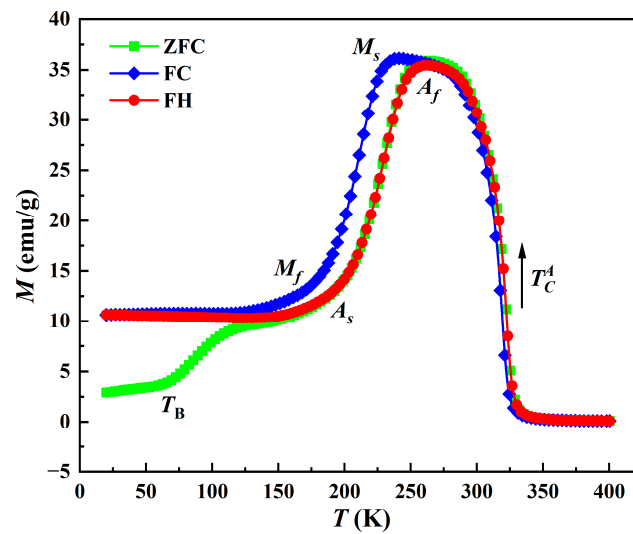


Figure 4. Temperature dependence of magnetization of the virgin sample measured under a magnetic field of 500 Oe.

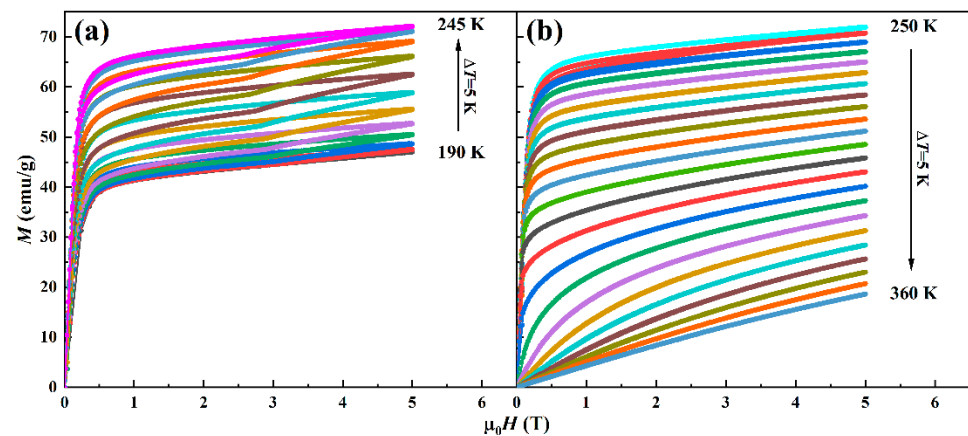


Figure 5. Selected isothermal magnetization curves under different temperatures with an applied magnetic field up to 5 T according to the thermomagnetic curves. (a) Around martensitic transformation. (b) Around magnetic transformation.

In order to further investigate the magnetization behavior at low temperatures, the hysteresis loops of the alloy at different temperatures were measured after cooling from 300 K under a 500 Oe field. As shown in Figure 6, the hysteresis loops obviously shift to the negative field at 2 K and 20 K, which confirms the behavior of the EB effect at low temperatures. The exchange bias field H_E shift is almost invisible at 65 K and disappears completely above this temperature, so it is confirmed as the blocking temperature T_B in the ZFC curve. This effect is associated with unidirectional anisotropy caused by the noncollinear coupling between the FM and AFM interfaces in a martensitic phase separation state. As the temperature increases, the pinning effect of AFM on the FM by the microscopic torque decreases, and the exchange bias field disappears at the blocking temperature [7,36].

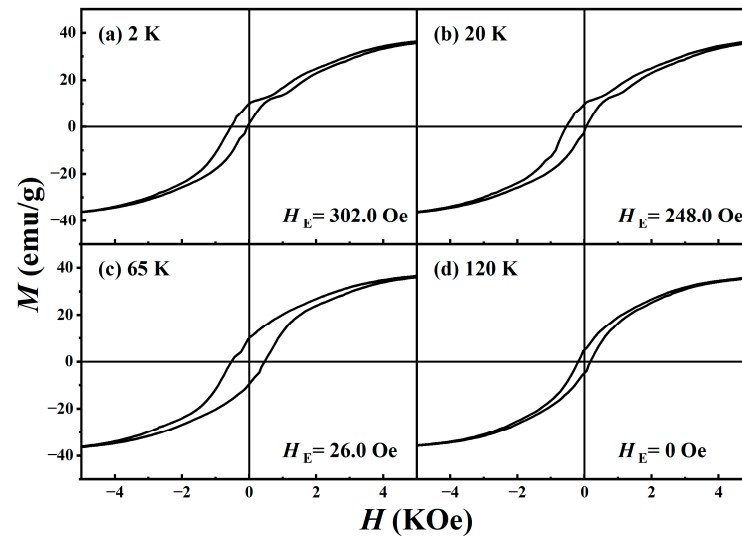


Figure 6. Magnetization hysteresis loops measured at (a) $T = 2$ K, (b) $T = 20$ K, (c) $T = 65$ K, and (d) $T = 120$ K.

The magnetocaloric effect was estimated by the values ΔS_M calculated from M - H curves data based on Maxwell's thermodynamic relation [6]:

$$\Delta S_M(T, \Delta H) = \mu_0 \int_0^H \left(\frac{\partial M}{\partial T} \right)_H dH \quad (1)$$

the temperature dependence of ΔS_M under several magnetic fields is described in Figure 7. The inset is the HL with a magnetic field change of 5 T, that is, the area surrounded by isothermal magnetization loops. IMCE and conventional MCE are confirmed by respective peaks, the maximum ΔS_M attained is 3.5 J/kg·K, attributable to the structural transformation, and -4.1 J/kg·K on account of magnetic transformation, under the magnetic field change of 5 T. Although limited, the most significant feature is the large temperature widths (60 K and more than 100 K) occupied by two characteristic peaks. This brings about a wide operating temperature window for magnetic refrigeration materials, which is important for applications.

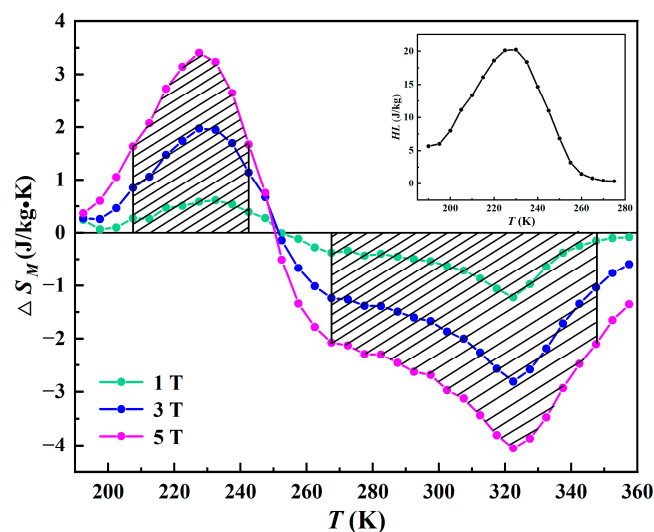


Figure 7. Temperature dependence of magnetic entropy change under several magnetic fields. Inset: HL as a function of temperature for a magnetic field change of 5 T.

The refrigeration capacity (RC) is another essential parameter for appraising the MCE. It represents the amount of thermal energy transmitted between cold and hot sources in the ideal thermodynamic cycle, and can be defined with the following formula [37]:

$$RC = \int_{T_c}^{T_h} \Delta S_M(T) dT \quad (2)$$

where T_c and T_h are determined as the full-width half the maximum peak (FWHM) of the ΔS_M - T curve, which corresponds to temperatures of cold and hot sources. So, the interval $\delta T_{FWHM} = T_h - T_c$ is also defined as the useful operating temperature range of MCE materials. The calculated values of RC for IMCE and MCE are 94 J/kg and 234 J/kg under the magnetic field change of 5 T, as shown in the shaded parts of Figure 7. After subtracting the average HL (14 J/kg for structural transformation and 0 for magnetic transformation, respectively), the total effective refrigerant capacity RC_{eff}^{total} amounts to 314 J/kg. This is comparable to $Ni_{43}Mn_{46}Sn_{11}$ ($RC_{eff}^{IMCE} = 82.9$ J/kg, 5 T) [38], $Ni_{49.8}Co_{1.2}Mn_{33.5}In_{15.5}$ ($RC_{eff}^{IMCE} = 76.6$ J/kg, 5 T) [39], $Ni_{45}Mn_{39}Sb_{12}Co_4$ ($RC_{eff}^{IMCE} = 118.86$ J/kg, 7 T) [40], $Ni_{47}Mn_{40}Sn_{13}$ ($RC_{eff}^{total} = 269$ J/kg, 5 T) [41], $Ni_{44.9}Fe_{4.3}Mn_{38.3}Sn_{12.5}$ ($RC_{eff}^{total} = 310.5$ J/kg, 5 T) [42], and much greater than $Ni_{50}Mn_{37}Sn_{13}$ ($RC^{total} = 105$ J/kg, 5 T) [43]. High effective refrigeration capacity benefits from small HL and large temperature ranges, and the resulting potential improvement in magnetic refrigeration cyclic stability and broad operating temperature window are advantageous for applications of magnetic refrigeration materials.

In addition, to reveal the effect of magnetic crystal orientation, the magnetic properties of the sample were measured under a magnetic field perpendicular to CGD (not shown here) and all the results were not significantly different compared to the measurements with a parallel magnetic field. This indicates that the Ni–Mn–Sn unidirectional crystal prepared in this study has a low magnetic crystal anisotropy.

3.3. Electrical Properties

To further explore the effect of phase transformations on electronic transport characteristics, the temperature dependence of electrical resistivity has been measured under the action of 0 and 5 T magnetic fields, as shown in Figure 8. Obviously, the resistivity shows a jump in the temperature range of 170 K to 250 K. This results from the fact that the structural phase transformation would change the electrical transport characteristics of the sample, and the parameters for MT are basically consistent with the magnetization measurement in Figure 4. One reason for the resistance change is the difference in the intensity of scattering between electrons and phonons inside the crystal in two phases [44]. On the other hand, the variation of density of states on the Fermi surface during phase transformation is another factor [45,46]. In addition, the characteristic temperatures of phase transformation shift to low temperature by about 10 K under the condition of a 5 T applied magnetic field, which can be ascribed to the fact that the ferromagnetic stability of high-temperature parent phase would be improved with the introduction of a magnetic field, leading to the decrease in phase transformation temperatures. MR was calculated using the formula $MR = [\rho(H) - \rho(0)]/\rho(0)$, where $\rho(H)$ and $\rho(0)$ are the resistivity under a 5 T magnetic field and zero field respectively, as shown in the inset of Figure 8. A maximum of about -18% MR (205 K) and hysteresis was observed during both cooling and heating procedures. Negative MR is on account of the transformation from the high resistance martensite to low resistance austenite phase induced by magnetic field. Due to a transition from a less ordered state to more ordered state during heating reducing residual resistivity associated with the disorder, the maximum MR obtained during the heating procedure is smaller than that of the cooling procedure [47].

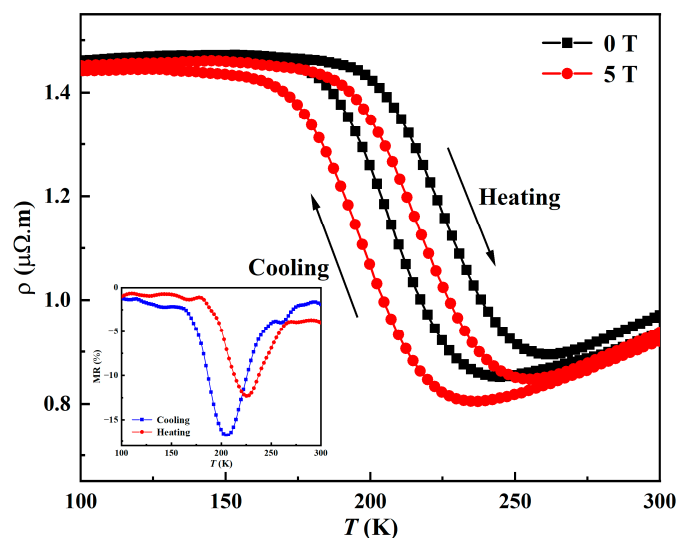


Figure 8. Electrical resistivity as a function of temperature under 0 and 5 T magnetic fields. Inset: Magnetoresistance vs. temperature curves under 5 T magnetic fields.

3.4. Mechanical Properties

The inherent brittleness of Mn-rich Ni–Mn-based Heusler alloys is the key factor hindering their engineering applications. Figure 9 shows the stress–strain curves of the materials compressed to fracture at room temperature; the SEM fracture cross-section is shown in the insets. A small cylinder with a diameter of 3 mm and a length of 7 mm was cut from the sample rod for a compression experiment. The direction of stress applied during compression of [001]-oriented sample is parallel to the SD with a constant speed of 0.15 mm/min. As a contrast, we performed a compression test under the same conditions on a non-oriented polycrystalline sample. The result shows that the maximum compressive strength of the [001]-oriented sample is 1068 MPa and the fracture strain is 9.0%, which is increased by 63.8% and 114%, respectively, compared with 652 MPa and 4.2% of the polycrystalline sample. This mechanical property is excellent compared with previous studies on polycrystalline Ni–Mn-based alloys, and it can be compared with some Co-based alloys [48,49]. The reason can be attributed to the fact that directional solidification eliminates the transverse grain boundaries sensitive to void and crack in the crystallization process, leaving a negligible amount of longitudinal grain boundaries, and making the grain boundaries parallel to the stress axis, thus improving the unidirectional mechanical properties of the material. The microstructure texture can help encourage strain coordination between grain boundaries and decrease the stress concentrations at triple junctions [50]. Furthermore, Chen et al. found unprecedented hyperelasticity in [001]-oriented Ni–Co–Fe–Ga crystal and explained that it is probably because of the lack of fluidity of the habit plane interfaces along with its remarkable lattice anti-slip resistance [51], which may also apply to our material. The good mechanical properties also provide the basis for its possible elastocaloric effect (eCE) [52,53], which deserves further experimental study. Based on the fracture morphologies, the non-oriented sample presents an intergranular crack of intermetallics with fracture flake and smooth crystal interface, and the fracture mechanism of the [001]-oriented sample is a mixture of intergranular fracture and transgranular fracture. Thus, the ductility of the sample is enhanced. It is unambiguously certain that this unidirectional crystal growth method can improve the mechanical properties of Ni–Mn-based alloys and broaden their application prospects.

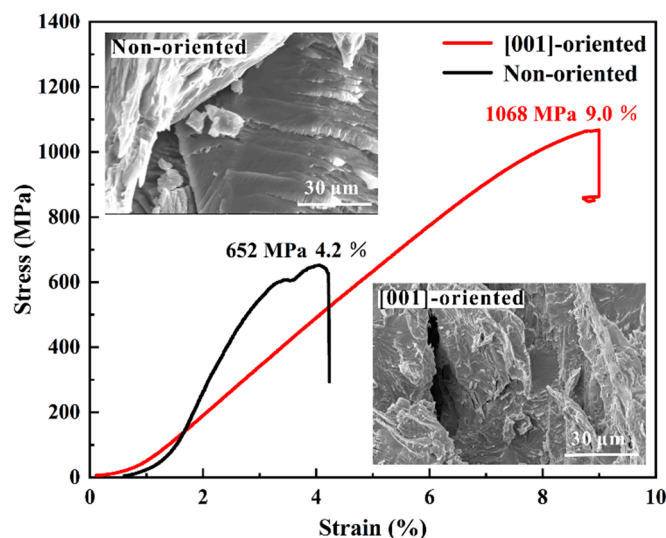


Figure 9. Compressive stress–strain curves at room temperature. Insets: SEM fractographs.

4. Conclusions

In the present work, a $\text{Ni}_{50}\text{Mn}_{36}\text{Sn}_{14}$ Heusler alloy with unidirectional crystal was grown by the directional solidification method. The crystal exhibits a single austenite phase $L2_1$ cubic structure at room temperature, and the lattice parameter is $a = 5.997 \text{ \AA}$. The total effective magnetic refrigerant capacity amounts to about 314 J/kg under the magnetic field change of 5 T , and the broad operating temperature window and small magnetic hysteresis loss are significant conditions for improving the refrigerant performance. The exchange bias field of 302 Oe was observed (2 K , 500 Oe field cooling) as a result of the coexistence of FM and AFM interactions at low temperatures. It is noteworthy that the magnetic properties of $[001]$ -oriented Ni–Mn–Sn unidirectional crystal do not exhibit magnetic anisotropy. Measurements of magnetization and resistivity characterize the phase transformation of the sample and show -18% magnetoresistance (205 K , 5 T) during the cooling procedure. Furthermore, the ultimate compression test shows that the mechanical properties of the $[001]$ -oriented sample (fracture strength and strain are 1068 MPa and 9.0% , respectively) are significantly better than the polycrystalline sample, which could extend the engineering applications of such alloys.

Author Contributions: Conceptualization, investigation, discussion of results, writing—original draft, H.S. and C.J.; sample preparation, Y.S. and S.Y.; equipment assistance, L.H.; data analysis, Y.Z. and H.Z.; result discussion, methodology, T.B., S.Y. and T.Z.; funding acquisition, supervision, C.J. and W.R. All authors have read and agreed to the published version of the manuscript.

Funding: This work was financially supported by the National Natural Science Foundation of China (Nos. 12274278, 12074241, 62171268), Independent Research and Development Project of State Key Laboratory of Advanced Special Steel, Shanghai Key Laboratory of Advanced Ferrometallurgy, Shanghai University (SKLASS 2020-Z07).

Institutional Review Board Statement: Not applicable.

Informed Consent Statement: Not applicable.

Data Availability Statement: Data are available from the authors upon reasonable request.

Conflicts of Interest: The authors declare no conflict of interest.

References

1. Sutou, Y.; Imano, Y.; Koeda, N.; Omori, T.; Kainuma, R.; Ishida, K.; Oikawa, K. Magnetic and martensitic transformations of Ni–Mn–X ($X = \text{In, Sn, Sb}$) ferromagnetic shape memory alloys. *Appl. Phys. Lett.* **2004**, *85*, 4358–4360. [[CrossRef](#)]
2. Planes, A.; Mañosa, L.; Acet, M. Magnetocaloric effect and its relation to shape-memory properties in ferromagnetic Heusler alloys. *J. Phys. Condens. Matter* **2009**, *21*, 233201. [[CrossRef](#)] [[PubMed](#)]

3. Du, J.; Zheng, Q.; Ren, W.J.; Feng, W.J.; Liu, X.G.; Zhang, Z.D. Magnetocaloric effect and magnetic-field-induced shape recovery effect at room temperature in ferromagnetic Heusler alloy Ni-Mn-Sb. *J. Phys. D Appl. Phys.* **2007**, *40*, 5523–5526. [[CrossRef](#)]
4. Wederni, A.; Ipatov, M.; Pineda, E.; Escoda, L.; González, J.M.; Khitouni, M.; Suñol, J.J. Martensitic transformation, thermal analysis and magnetocaloric properties of Ni-Mn-Sn-Pd alloys. *Processes* **2020**, *8*, 1582. [[CrossRef](#)]
5. Dahal, B.; Huber, C.; Zhang, W.Y.; Valloppilly, S.; Huh, Y.; Kharel, P.; Sellmyer, D. Effect of partial substitution of In with Mn on the structural, magnetic, and magnetocaloric properties of Ni₂Mn_{1+x}In_{1-x} Heusler alloys. *J. Phys. D Appl. Phys.* **2019**, *52*, 425305. [[CrossRef](#)]
6. Krenke, T.; Duman, E.; Acet, M.; Wassermann, E.F.; Moya, X.; Mañosa, L.; Planes, A. Inverse magnetocaloric effect in ferromagnetic Ni-Mn-Sn alloys. *Nat. Mater.* **2005**, *4*, 450–454. [[CrossRef](#)] [[PubMed](#)]
7. Khan, M.; Dubenko, I.; Stadler, S.; Ali, N. Exchange bias in bulk Mn rich Ni-Mn-Sn Heusler alloys. *J. Appl. Phys.* **2007**, *102*, 113914. [[CrossRef](#)]
8. Çakır, A.; Acet, M.; Farle, M. Exchange bias caused by field-induced spin reconfiguration in Ni-Mn-Sn. *Phys. Rev. B* **2016**, *93*, 094411. [[CrossRef](#)]
9. Chabri, T.; Ghosh, K.; Mukherjee, D.; Nath, T.K. Role of interplay of austenite and martensite phase fractions on the magnetocaloric and magnetoelastic effects across the martensite transition in Ni₄₅Mn₄₄Sn₇In₄ Heusler alloy near room temperature. *J. Appl. Phys.* **2020**, *128*, 215106. [[CrossRef](#)]
10. Chabria, T.; Barman, A.; Chatterjee, S.; Mollick, S.A.; Nath, T.K.; Mukherjee, D. Effects of transitional hysteresis on the large magnetocaloric and magnetoelastic properties of Ni-Mn-Co-Sn Heusler alloy. *J. Alloys Compd.* **2021**, *863*, 158485. [[CrossRef](#)]
11. Li, L.W.; Yan, M. Recent progress in the development of RE₂TMTM'O₆ double perovskite oxides for cryogenic magnetic refrigeration. *J. Mater. Sci. Technol.* **2023**, *136*, 1–12. [[CrossRef](#)]
12. Xu, P.; Hu, L.; Zhang, Z.Q.; Wang, H.F.; Li, L.W. Electronic structure, magnetic properties and magnetocaloric performance in rare earths (RE) based RE₂BaZnO₅ (RE = Gd, Dy, Ho, and Er) compounds. *Acta Mater.* **2022**, *236*, 118114. [[CrossRef](#)]
13. Zhang, Y.K.; Li, S.; Hu, L.; Wang, X.H.; Li, L.W.; Yan, M. Excellent magnetocaloric performance in the carbide compounds RE₂Cr₂C₃ (RE = Er, Ho, and Dy) and their composites. *Mater. Today Phys.* **2022**, *27*, 100786. [[CrossRef](#)]
14. Zheng, H.X.; Wang, W.; Xue, S.C.; Zhai, Q.J.; Frenzel, J.; Luo, Z.P. Composition-dependent crystal structure and martensitic transformation in Heusler Ni-Mn-Sn alloys. *Acta Mater.* **2013**, *61*, 4648–4656. [[CrossRef](#)]
15. Ameer, R.; Chemingui, M.; Bachaga, T.; Escoda, L.; Khitouni, M.; Suñol, J.J. Martensitic transformation and crystalline structure of Ni₅₀Mn_{50-x}Sn_x melt-spun Heusler Alloys. *Crystals* **2020**, *10*, 853. [[CrossRef](#)]
16. Krenke, T.; Acet, M.; Wassermann, E.F. Martensitic transitions and the nature of ferromagnetism in the austenitic and martensitic states of Ni-Mn-Sn alloys. *Phys. Rev. B* **2005**, *72*, 014412. [[CrossRef](#)]
17. Wang, B.M.; Liu, Y.; Ren, P.; Xia, B.; Ruan, K.B.; Yi, J.B.; Ding, J.; Li, X.G.; Wang, L. Large exchange bias after zero-field cooling from an unmagnetized state. *Phys. Rev. Lett.* **2011**, *106*, 077203. [[CrossRef](#)] [[PubMed](#)]
18. Ma, L.; Wang, W.H.; Lu, J.B.; Li, J.Q.; Zhen, C.M.; Hou, D.L.; Wu, G.H. Coexistence of reentrant-spin-glass and ferromagnetic martensitic phases in the Mn₂Ni_{1.6}Sn_{0.4} Heusler alloy. *Appl. Phys. Lett.* **2011**, *99*, 182507. [[CrossRef](#)]
19. Liao, P.; Jing, C.; Wang, X.L.; Yang, Y.J.; Zheng, D.; Li, Z.; Kang, B.J.; Deng, D.M.; Cao, S.X.; Zhang, J.C.; et al. Strongly enhanced antiferromagnetism and giant spontaneous exchange bias in Ni₅₀Mn₃₆Co₄Sn₁₀ Heusler alloy. *Appl. Phys. Lett.* **2014**, *104*, 092410. [[CrossRef](#)]
20. Sharma, J.; Suresh, K.G. Observation of giant exchange bias in bulk Mn₅₀Ni₄₂Sn₈ Heusler alloy. *Appl. Phys. Lett.* **2015**, *106*, 072405. [[CrossRef](#)]
21. Wederni, A.; Ipatov, M.; Pineda, E.; Suñol, J.J.; Escoda, L.; Maria González, J.; Alleg, S.; Khitouni, M.; Żuberek, R.; Chumak, O.; et al. Magnetic properties, martensitic and magnetostructural transformations of ferromagnetic Ni-Mn-Sn-Cu shape memory alloys. *Appl. Phys. A* **2020**, *126*, 320. [[CrossRef](#)]
22. Yang, J.J.; Li, Z.B.; Yang, B.; Yan, H.L.; Cong, D.Y.; Zhao, X.; Zuo, L. Effects of Co and Si co-doping on magnetostructural transformation and magnetocaloric effect in Ni-Mn-Sn based alloys. *J. Alloys Compd.* **2021**, *892*, 162190. [[CrossRef](#)]
23. Wang, L.B.; Xuan, H.C.; Liu, S.L.; Cao, T.; Xie, Z.G.; Liang, X.H.; Chen, F.H.; Zhang, K.W.; Feng, L.; Han, P.D.; et al. Enhanced elastocaloric effect and mechanical properties of Gd-doped Ni-Mn-Sn-Gd ferromagnetic shape memory alloys. *J. Alloys Compd.* **2020**, *846*, 156313. [[CrossRef](#)]
24. Qian, H.Y.; Dahal, B.; Halbritter, L.; Hu, J.; Huh, Y.; Kharel, P. Structural, magnetic and magnetocaloric properties of Ni₄₃Mn_{46-x}Fe_xSn₁₁ (x = 0, 6, 8, 10) alloys. *AIP Adv.* **2019**, *9*, 035005. [[CrossRef](#)]
25. Wójcik, A.; Maziarsz, W.; Szczerba, M.; Kowalczyk, M.; Cesari, E.; Dutkiewicz, J. Structure and inverse magnetocaloric effect in Ni-Co-Mn-Sn(Si) Heusler alloys. *Intermetallics* **2018**, *100*, 88–94. [[CrossRef](#)]
26. Ghosh, A.; Mandal, K. Effect of structural disorder on the magnetocaloric properties of Ni-Mn-Sn alloy. *Appl. Phys. Lett.* **2014**, *104*, 031905. [[CrossRef](#)]
27. Bachaga, T.; Zhang, J.; Ali, S.; Suñol, J.J.; Khitouni, M. Impact of annealing on martensitic transformation of Mn₅₀Ni_{42.5}Sn_{7.5} shape memory alloy. *Appl. Phys. A* **2019**, *125*, 146. [[CrossRef](#)]
28. Żuberek, R.; Chumak, O.M.; Nabiałek, A.; Chojnacki, M.; Radelytskiy, I.; Szymczak, H. Magnetocaloric effect and magnetoelastic properties of NiMnGa and NiMnSn Heusler alloy thin films. *J. Alloys Compd.* **2018**, *748*, 1–5. [[CrossRef](#)]
29. Ling, Y.C.; Hu, Y.; Wang, H.B.; Niu, B.; Chen, J.W.; Liu, R.B.; Yuan, Y.; Wang, G.Y.; Wu, D.; Xu, M.X.; et al. Strain control of phase transition and exchange bias in flexible Heusler alloy thin films. *ACS Appl. Mater. Interfaces* **2021**, *13*, 24285–24294. [[CrossRef](#)]

30. Dadda, K.; Alleg, S.; Saurina, J.; Escoda, L.; Suñol, J.J. Structure, microstructure, and magnetic properties of melt spun $\text{Ni}_{50}\text{Mn}_{50-x}\text{In}_x$ ribbons. *Magnetochemistry* **2021**, *7*, 63. [[CrossRef](#)]
31. Ullakko, K.; Huang, J.K.; Kantner, C.; O'Handley, R.C.; Kokorin, V.V. Large magnetic-field-induced strains in Ni_2MnGa single crystals. *Appl. Phys. Lett.* **1996**, *69*, 1966. [[CrossRef](#)]
32. Ren, J.; Li, H.W.; Yu, J.K.; Feng, S.T.; Zhai, Q.J.; Fu, J.X.; Luo, Z.P.; Zheng, H.X. Enhanced magnetocaloric effect in Heusler Ni-Mn-Sn unidirectional crystal. *J. Alloys Compd.* **2015**, *634*, 65–69. [[CrossRef](#)]
33. Zhang, G.Y.; Li, Z.B.; Yang, J.J.; Yang, B.; Wang, D.H.; Zhang, Y.D.; Esling, C.; Hou, L.; Li, X.; Zhao, X.; et al. Giant elastocaloric effect in a Mn-rich $\text{Ni}_{44}\text{Mn}_{46}\text{Sn}_{10}$ directionally solidified alloy. *Appl. Phys. Lett.* **2020**, *116*, 023902. [[CrossRef](#)]
34. Niu, Y.R.; Chen, H.Y.; Zhang, X.Y.; Li, S.W.; Cong, D.Y.; Ma, T.Y.; Li, S.L.; Lin, J.P.; Wang, Y.D. Achieving excellent superelasticity and extraordinary elastocaloric effect in a directionally solidified Co-V-Ga alloy. *Scr. Mater.* **2021**, *204*, 114123. [[CrossRef](#)]
35. Li, Z.Z.; Li, Z.B.; Li, D.; Yang, J.J.; Yang, B.; Hu, Y.; Wang, D.H.; Zhang, Y.D.; Esling, C.; Zhao, X.; et al. Achieving a broad refrigeration temperature region through the combination of successive caloric effects in a multiferroic $\text{Ni}_{50}\text{Mn}_{35}\text{In}_{15}$ alloy. *Acta Mater.* **2020**, *192*, 52–59. [[CrossRef](#)]
36. Li, Z.; Jing, C.; Chen, J.P.; Yuan, S.J.; Cao, S.X.; Zhang, J.C. Observation of exchange bias in the martensitic state of $\text{Ni}_{50}\text{Mn}_{36}\text{Sn}_{14}$ Heusler alloy. *Appl. Phys. Lett.* **2007**, *91*, 112505. [[CrossRef](#)]
37. Provenzano, V.; Shapiro, A.J.; Shull, R.D. Reduction of hysteresis losses in the magnetic refrigerant $\text{Gd}_5\text{Ge}_2\text{Si}_2$ by the addition of iron. *Nature* **2004**, *429*, 853–857. [[CrossRef](#)]
38. Zhang, Y.; Zheng, Q.; Xia, W.X.; Zhang, J.; Du, J.; Yan, A. Enhanced large magnetic entropy change and adiabatic temperature change of $\text{Ni}_{43}\text{Mn}_{46}\text{Sn}_{11}$ alloys by a rapid solidification method. *Scr. Mater.* **2015**, *104*, 41–44. [[CrossRef](#)]
39. Huang, L.; Cong, D.Y.; Ma, L.; Nie, Z.H.; Wang, Z.L.; Suo, H.L.; Ren, Y.; Wang, Y.D. Large reversible magnetocaloric effect in a Ni-Co-Mn-In magnetic shape memory alloy. *Appl. Phys. Lett.* **2016**, *108*, 032405. [[CrossRef](#)]
40. Kavita, S.; Ramakrishna, V.V.; Behara, S.; Suganthi, S.; Kar, D.N.; Thomas, T.; Ramesh, T.; Sethupathi, K.; Gopalan, R. Investigation of magnetocaloric and mechanical properties of $\text{Ni}_{49-x}\text{Mn}_{39}\text{Sb}_{12}\text{Co}_x$ alloys. *J. Alloys Compd.* **2020**, *847*, 156558. [[CrossRef](#)]
41. Varzaneh, A.G.; Kameli, P.; Amiri, T.; Ramachandran, K.K.; Mar, A.; Sarsari, I.A.; Luo, J.L.; Etsell, T.H.; Salamati, H. Effect of Cu substitution on magnetocaloric and critical behavior in $\text{Ni}_{47}\text{Mn}_{40}\text{Sn}_{13-x}\text{Cu}_x$ alloys. *J. Alloys Compd.* **2017**, *708*, 34–42. [[CrossRef](#)]
42. Zhang, H.H.; Qian, M.F.; Zhang, X.X.; Jiang, S.D.; Wei, L.S.; Xing, D.W.; Sun, J.F.; Geng, L. Magnetocaloric effect of Ni-Fe-Mn-Sn microwires prepared by melt-extraction technique. *Mater. Des.* **2017**, *114*, 1–9. [[CrossRef](#)]
43. Saha, R.; Nigam, A.K. Room temperature inverse magnetocaloric effect in Pd substituted $\text{Ni}_{50}\text{Mn}_{37}\text{Sn}_{13}$ Heusler alloys. *Physics B* **2014**, *448*, 263–266. [[CrossRef](#)]
44. Jing, C.; Yang, Y.J.; Li, Z.; Wang, X.L.; Kang, B.J.; Cao, S.X.; Zhang, J.C.; Zhu, J.; Lu, B. Tuning martensitic transformation and large magnetoresistance in $\text{Ni}_{50-x}\text{Cu}_x\text{Mn}_{38}\text{Sn}_{12}$ Heusler alloys. *J. Appl. Phys.* **2013**, *113*, 173902. [[CrossRef](#)]
45. Zhang, B.; Zhang, X.X.; Yu, S.Y.; Chen, J.L.; Cao, Z.X.; Wu, G.H. Giant magnetothermal conductivity in the Ni-Mn-In ferromagnetic shape memory alloys. *Appl. Phys. Lett.* **2007**, *91*, 012510. [[CrossRef](#)]
46. Sechovský, V.; Havela, L.; Prokeš, K.; Nakotte, H.; de Boer, F.R.; Brück, E. Giant magnetoresistance effects in intermetallic compounds (invited). *J. Appl. Phys.* **1994**, *76*, 6913. [[CrossRef](#)]
47. Singh, S.; Biswas, C. Magnetoresistance origin in martensitic and austenitic phases of $\text{Ni}_2\text{Mn}_{1+x}\text{Sn}_{1-x}$. *Appl. Phys. Lett.* **2011**, *98*, 212101. [[CrossRef](#)]
48. Tan, C.L.; Zhang, K.; Tian, X.H.; Cai, W. Effect of Gd addition on microstructure, martensitic transformation and mechanical properties of $\text{Ni}_{50}\text{Mn}_{36}\text{Sn}_{14}$ ferromagnetic shape memory alloy. *J. Alloys Compd.* **2017**, *692*, 288–293. [[CrossRef](#)]
49. Liu, K.; Yuan, Y.; Ma, S.C.; Feng, G.F.; Wan, D.J.; Wang, S.B.; Chen, C.C.; Luo, X.H.; Zhong, Z.C. Large elastocaloric effect around room temperature in directionally solidified $\text{Co}_{49}\text{Fe}_3\text{V}_{33}\text{Ga}_{15}$ superelastic alloy. *J. Alloys Compd.* **2021**, *884*, 161094. [[CrossRef](#)]
50. Huang, Y.J.; Hu, Q.D.; Bruno, N.M.; Chen, J.H.; Karaman, I.; Ross, J.H.; Li, J.G. Giant elastocaloric effect in directionally solidified Ni-Mn-In magnetic shape memory alloy. *Scr. Mater.* **2015**, *105*, 42–45. [[CrossRef](#)]
51. Chen, H.Y.; Wang, Y.D.; Nie, Z.H.; Li, R.G.; Cong, D.Y.; Liu, W.J.; Ye, F.; Liu, Y.Z.; Cao, P.Y.; Tian, F.Y.; et al. Unprecedented non-hysteretic superelasticity of [001]-oriented NiCoFeGa single crystals. *Nat. Mater.* **2020**, *19*, 712–718. [[CrossRef](#)] [[PubMed](#)]
52. Shen, Y.; Sun, W.; Wei, Z.Y.; Shen, Q.; Zhang, Y.F.; Liu, J. Orientation dependent elastocaloric effect in directionally solidified Ni-Mn-Sn alloys. *Scr. Mater.* **2019**, *163*, 14–18. [[CrossRef](#)]
53. Zhao, D.W.; Liu, J.; Feng, Y.; Sun, W.; Yan, A. Giant elastocaloric effect and its irreversibility in [001]-oriented $\text{Ni}_{45}\text{Mn}_{36.5}\text{In}_{13.5}\text{Co}_5$ meta-magnetic shape memory alloys. *Appl. Phys. Lett.* **2017**, *110*, 021906. [[CrossRef](#)]